

Direct measurement of electrostatic potentials at the atomic scale: A conceptual comparison between electron holography and scanning transmission electron microscopy

Florian Winkler^{a,*}, Juri Barthel^a, Rafal E. Dunin-Borkowski^{a,b}, Knut Müller-Caspary^{a,c}

^a Ernst Ruska-Centre for Microscopy and Spectroscopy with Electrons (ER-C), Forschungszentrum Jülich, Jülich 52425, Germany

^b Peter Grünberg Institute 5 (PGI-5), Forschungszentrum Jülich, Jülich 52425, Germany

^c 2nd Institute of Physics, RWTH Aachen University, Aachen 52074, Germany

ARTICLE INFO

Keywords:

Off-axis electron holography
Scanning transmission electron microscopy
Electrostatic potentials
Thermal diffuse scattering

ABSTRACT

Off-axis electron holography and first moment STEM are sensitive to electromagnetic potentials or fields, respectively. In this work, we investigate in what sense the results obtained from both techniques are equivalent and work out the major differences. The analysis is focused on electrostatic (Coulomb) potentials at atomic spatial resolution. It is shown that the probe-forming/objective aperture strongly affects the reconstructed electrostatic potentials and that, as a result of the different illumination setups, dynamical diffraction effects show a specific response with increasing specimen thickness. It is shown that thermal diffuse scattering is negligible for a wide range of specimen thicknesses, when evaluating the first moment of diffraction patterns.

1. Introduction

In transmission electron microscopy (TEM), a thin object is exposed to a beam of high energy electrons. The interaction between the incident electron beam and the specimen modifies both amplitude and phase of the electron wavefunction, as described mathematically by a relativistically corrected time-invariant Schrödinger equation. Especially for very thin objects most of the object information is transferred to the phase of the electron wavefunction. In conventional TEM, only the modulus squared of the wavefunction is recorded in the image plane. As a result, the phase information is lost completely in (nearly) aberration-free systems, or it is transferred to amplitude contrast in a complex manner in the presence of aberrations.

An established method to overcome this phase problem is off-axis electron holography (EH), in which both phase and amplitude of the wavefunction in the image plane can be recovered by recording an interference pattern formed by a Möllenstedt–Düker biprism [1,2]. Thus, phase information can be restored with up to atomic spatial resolution and interpreted in terms of the projected electrostatic potential under the right circumstances [3–6].

In addition, scanning TEM (STEM) experiences a rapid development in both instrumentation and methodology since a few years. In particular, the introduction of ultrafast detectors [7–11] has enabled the acquisition of two-dimensional (2D) diffraction patterns at each

position of the scanning probe. This is often referred to as 4D or momentum-resolved STEM (MRSTEM). Importantly, it laid the basis for quantitative differential phase contrast (DPC), in which the first moment of diffraction patterns is identified as the lateral momentum transferred to the STEM probe by the specimen. This will be referred to as first-moment STEM (FMSTEM) throughout this work. For thin objects where the phase object approximation (POA) holds, this has recently enabled the mapping of electric fields at the subatomic scale [12–14]. Furthermore, MRSTEM data allows for the application of techniques such as electron ptychography [15–17], from which both amplitude and phase of the object transmission function are recovered by exploring the full information in every diffraction pattern.

A measurement of the Coulomb potential $V(\vec{r})$ and electric field $\vec{E}(\vec{r})$ with EH and FMSTEM, respectively, thus creates an interesting situation from a fundamental scientific and methodological point of view. Both these quantities are uniquely connected via

$$\vec{E}(\vec{r}) = -\vec{\nabla}V(\vec{r}), \quad (1)$$

where $\vec{\nabla}$ is the nabla operator. Hence, the measurements with EH and FMSTEM should, except for an additive constant, ideally yield the same results under identical (comparable) optical setups after differentiation or integration, respectively. However, a closer look at the concepts behind both techniques quickly shows that their comparison is rather

* Corresponding author.

E-mail address: f.winkler@fz-juelich.de (F. Winkler).

complex. Some of the most urgent aspects to be elucidated should, for example, address:

1. The meaning and definition of identical optical setups.
2. Conceptual differences as to the interpretation of results: One interpretation argues with a quantum-mechanical wavefunction (EH), the other with an intensity distribution (MRSTEM).
3. The impact of dynamical diffraction. Given a plane wave illumination in EH and a conical illumination in STEM, are the ranges for the validity of the POA different for both techniques?
4. The influence of thermal diffuse scattering (TDS). EH is a perfect filter for TDS, whereas it is usually unavoidable in STEM performed at room temperature, even when using contemporary energy filters. To which extent does TDS affect the results of FMSTEM in dependence on specimen thickness?
5. Practical aspects: How do the experimental setups for both techniques limit or enable certain studies? Which requirements exist concerning the stability of microscope hardware, and which precision can be achieved for the measurement of a certain parameter, e.g., the Coulomb potential, when using the same (total) dose?

An in-depth answer to all these aspects is beyond the scope of a single study, which is why this work is organised as follows. We present a detailed quantitative analysis of aspects 1–4 in a theoretical study with extensive simulations, whereas we discuss aspect 5 qualitatively at the end of the manuscript. This way was chosen because it is possible to focus on the conceptual comparison as all parameters of the simulation are known. In particular, we circumvent difficulties that arise, e.g., from the different impact of the point spread functions of the detectors used for acquisition during the explicit comparison. On the one hand, such factors play a key role in practice. On the other hand, this would make the methodological comparison dependent on the respective state of technology which we regard as unfavourable in view of the rapid pace of innovations.

2. Theory

Let us start by recalling the basic mathematical description of the signal formation in TEM assuming perfect coherence and elastic scattering for simplicity. The incident electron wavefunction Ψ_{in} interacts with the Coulomb potential $V(x, y, z)$ of the specimen so as to form $\Psi_{\text{obj}}(\vec{r})$, the wavefunction present at the exit-plane of the investigated object. Here, $\vec{r} = (x, y)$ denotes a 2D real-space vector perpendicular to the optical axis of the microscope, which is along z . Whereas in EH $\Psi_{\text{in}}(\vec{r}) = 1$ is typically a plane wave, a convergent electron probe is formed by the condenser system of the microscope in STEM, which is described by the expression

$$\Psi_{\text{in}}(\vec{r}, \vec{r}_0) = \mathcal{F}^{-1} \left[B(\vec{k}) e^{-i\chi(\vec{k})} \right] \otimes \delta(\vec{r} - \vec{r}_0), \quad (2)$$

where \mathcal{F} describes the Fourier transform and \mathcal{F}^{-1} denotes an inverse Fourier transform. The Fourier space vector \vec{k} is conjugated to \vec{r} , $B(\vec{k})$ is a (typically circular) aperture function, and $\chi(\vec{k})$ is the aberration function [18]. The last term in Eq. (2) is responsible for scanning the probe across the sample, where the probe position is given by \vec{r}_0 . The symbol \otimes denotes a convolution and $\delta(\vec{r})$ is the Dirac delta function. Throughout this work, Fourier transformed quantities are denoted solely by their corresponding spatial variable (\vec{k}), which means that the real space function $f(\vec{r})$ is connected to $f(\vec{k})$ via Fourier transform.

In the following, we will briefly summarise the basic principles of EH and FMSTEM, in order to highlight under which conditions electrostatic potentials or fields, respectively, can be obtained from a direct interpretation of experimental data. This is typically only valid under certain approximations for the interaction of the electron beam with the

specimen, such as the POA. In this case it is assumed that the interaction with the specimen causes only a phase shift of the incident electron wavefunction, such that

$$\Psi_{\text{obj}}(\vec{r}) = \Psi_{\text{in}}(\vec{r}) e^{iC_E V_{\text{proj}}(\vec{r})}, \quad (3)$$

where V_{proj} is the projection of $V(x, y, z)$ along the electron beam direction and C_E is the interaction constant that only depends on the electron energy. It must be stressed that the phase of the electron wavefunction is typically only proportional to the projected potential for extremely thin objects, which then allows for a straightforward quantitative interpretation of the measured phase in terms of an electrostatic potential with physical meaning. Elucidating up to which thicknesses EH and FMSTEM, respectively, can be interpreted within the POA, is therefore an essential focus of this study.

2.1. Off-axis electron holography

An off-axis electron hologram is formed by interfering two coherent waves by means of an electrostatic biprism [1,2]. Whereas one wave is transmitted through the specimen, and therefore carries information about the investigated object, the so-called reference wave is transmitted (ideally) without further modification through vacuum. Both waves are tilted towards each other by applying a positive voltage to the biprism, forming the hologram in the image plane. It is then possible to reconstruct the image wavefunction Ψ_{ima} from the hologram by means of Fourier optics [19]. The reconstructed wavefunction is given by the expression

$$\begin{aligned} \Psi_{\text{rec}}(\vec{r}) &= \Psi_{\text{ima}}(\vec{r}) \otimes B(\vec{r}) \\ &= \mathcal{F} \left[\Psi_{\text{obj}}(\vec{k}) e^{-i\chi(\vec{k})} \right] \otimes B(\vec{r}), \end{aligned} \quad (4)$$

where $B(\vec{r})$ is obtained by an inverse Fourier transform of the aperture function $B(\vec{k})$ that yields essentially a Bessel function of the first kind. The spatial frequency limitation can either be achieved by a physical (objective) aperture, which is often unnecessary, as the effects of partial spatial coherence and thermal vibrations of the specimen directly limit the spatial resolution, or by a digital reconstruction aperture required to separate the sideband from the centerband in the spectrum of the hologram. Whereas a deconvolution of the aperture function is usually not possible in general, the effect of coherent aberrations can be sufficiently eliminated [20]. Accurate a-posteriori aberration correction however requires precise knowledge of the aberration coefficients, which often presents a challenge in quantitative EH. Several approaches have already been demonstrated to solve this problem, even for purely crystalline samples, for example by forward modelling of the electron optical imaging process or by symmetry arguments [20–25].

We will thus assume in the following that coherent aberrations are absent, so that we can neglect this term for our further analysis:

$$\Psi_{\text{rec}}(\vec{r}) = \Psi_{\text{obj}}(\vec{r}) \otimes B(\vec{r}). \quad (6)$$

Under conditions in which the phase of the object wavefunction is proportional to the projected electrostatic potential and no amplitude modulation is present, such as in the POA, we obtain

$$\Psi_{\text{rec}}(\vec{r}) = e^{iC_E V_{\text{proj}}(\vec{r})} \otimes B(\vec{r}). \quad (7)$$

In this equation, there is no explicit occurrence of a convolution between $V_{\text{proj}}(\vec{r})$ and $B(\vec{r})$, which seemingly points towards the necessity for a Taylor expansion of the exponential, i.e., the weak phase approximation. Eq. (7) can be approximated by

$$\Psi_{\text{rec}}(\vec{r}) \approx e^{iC_E V_{\text{proj}}(\vec{r})} \otimes B(\vec{r}) = e^{iC_E V_{\text{rec}}^{\text{EH}}(\vec{r})}, \quad (8)$$

which we verified by numerical calculations. This approximation is sufficiently accurate for convolutions with circular apertures and yields

best accuracies for potentials with a small height, i.e., atomic potentials with small values of $C_E V_{\text{proj}}$, which corresponds to thin and/or light atomic columns. For typical values of aperture sizes, peak heights and widths of atomic potentials used in this work, the error is typically below 1 %. We can then calculate the reconstructed projected potential $V_{\text{rec}}^{\text{EH}}(\vec{r})$ from the phase of the image plane wavefunction.

2.2. First-moment STEM

In MRSTEM, a 2D Fraunhofer diffraction pattern is recorded at every scan position \vec{r}_0 , as given by the modulus squared of the object wavefunction in Fourier space

$$I_{\text{STEM}}(\vec{k}, \vec{r}_0) = \left| \Psi_{\text{obj}}(\vec{k}, \vec{r}_0) \right|^2, \quad (9)$$

which therefore yields a 4D data set with two dimensions in real space \vec{r}_0 and two dimensions in reciprocal space \vec{k} . Within the POA (c.f. Eq. (3)), we can write the (real space) object wavefunction present at scan position \vec{r}_0 as

$$\Psi_{\text{obj}}(\vec{r}, \vec{r}_0) = \Psi_{\text{in}}(\vec{r}, \vec{r}_0) e^{iC_E V_{\text{proj}}(\vec{r})}. \quad (10)$$

Information about electric fields can be extracted from such a 4D data set by calculating the first moment of the diffraction patterns, effectively reducing the data set to a 2D vector field [12]. Here, the first moment of the diffraction pattern represents the average lateral momentum $\langle \vec{p} \rangle(\vec{r}_0)$ transferred to the probe, which can be written as the quantum mechanical expectation value in real space, according to the expression

$$\langle \vec{p} \rangle(\vec{r}_0) = -i\hbar \iint \Psi_{\text{obj}}^*(\vec{r}, \vec{r}_0) \vec{\nabla} \Psi_{\text{obj}}(\vec{r}, \vec{r}_0) d\vec{r}. \quad (11)$$

The proportionality of $\langle \vec{p} \rangle(\vec{r}_0)$ and $E_{\text{proj}}(\vec{r})$ has already been demonstrated on the basis of Ehrenfests theorem [12] and within the POA in momentum space [13]. A derivation in real space is given here for completeness. If we assume a pure phase object we can insert Eq. (10) into Eq. (11), which yields

$$\begin{aligned} \langle \vec{p} \rangle(\vec{r}_0) &= -i\hbar \left(\iint \Psi_{\text{in}}^*(\vec{r}, \vec{r}_0) \vec{\nabla} \Psi_{\text{in}}(\vec{r}, \vec{r}_0) d\vec{r} \right. \\ &\quad \left. + \iint |\Psi_{\text{in}}(\vec{r}, \vec{r}_0)|^2 e^{-iC_E V_{\text{proj}}(\vec{r})} \vec{\nabla} e^{iC_E V_{\text{proj}}(\vec{r})} d\vec{r} \right) \end{aligned} \quad (12)$$

$$= \langle \vec{p} \rangle_{\text{probe}}(\vec{r}_0) + \langle \vec{p} \rangle_{\text{obj}}(\vec{r}_0). \quad (13)$$

The first summand in Eq. (12) represents the momentum transferred to the probe in vacuum $\langle \vec{p} \rangle_{\text{probe}}$. For a symmetric probe, such as the one defined by the circular aperture given here, this term is equal to zero. However, in general $\langle \vec{p} \rangle_{\text{probe}}$ can be non-zero and must be subtracted from all experimentally measured momentum transfers, in order to obtain the momentum transferred by the object $\langle \vec{p} \rangle_{\text{obj}}$. In the following we will assume a symmetric probe, such that $\langle \vec{p} \rangle_{\text{probe}} = 0$. Hence, we obtain

$$\langle \vec{p} \rangle(\vec{r}_0) = i\hbar \iint |\Psi_{\text{in}}(\vec{r}, \vec{r}_0)|^2 iC_E \vec{\nabla} V_{\text{proj}}(\vec{r}) d\vec{r} \quad (14)$$

$$= \hbar C_E (I_{\text{probe}} \otimes \vec{\nabla} V_{\text{proj}})(\vec{r}_0) \quad (15)$$

$$= \hbar C_E \vec{\nabla} V_{\text{rec}}^{\text{FM}}(\vec{r}_0), \quad (16)$$

where we defined the intensity distribution of the STEM probe as $I_{\text{probe}}(\vec{r}, \vec{r}_0) = |\Psi_{\text{in}}(\vec{r}, \vec{r}_0)|^2 \propto B^2(\vec{r})$.

In conclusion, the first moment in STEM diffraction patterns is, within the POA, proportional to the projection of the electric field along the incident beam direction ($E_{\text{proj}}(\vec{r}) = -\vec{\nabla} V_{\text{proj}}(\vec{r})$), convolved with the intensity distribution of the probe. We note that for the convolution given in Eq. (15), the probe intensity has to be inverted [13], i.e.

$I_{\text{probe}}(-\vec{r}_0)$, which however is only important for asymmetric probe shapes and which will be neglected in the following.

In the case of perfect aberration correction, the convolution kernel reduces to the squared Fourier transform of an aperture function, i.e., $B^2(\vec{r})$. A lateral integration of the electric field over the scanning coordinate \vec{r}_0 then yields the electrostatic potential $V_{\text{proj}}(\vec{r}_0)$ convolved with the probe intensity. As the integration cannot recover any constant offset to the potential, the mean inner potential of the specimen is lost. The integration can be performed by means of Fourier transforms, as outlined in Appendix A.

In contrast, the phase of the wavefunction obtained from EH is in good approximation proportional to the projected electrostatic potential convolved with $B(\vec{r})$, not $B^2(\vec{r})$. Therefore, EH and MRSTEM yield inherently different potentials already for a case where the POA would hold perfectly.

3. Methods

Electron diffraction is simulated using a multislice approach [26] as implemented within the Dr. Probe software package [27]. All simulations are performed for an electron energy of 300 keV. Elastic electron scattering potentials are taken from the tables of Weickenmeier and Kohl [28] and absorption into the inelastic TDS channel is modelled by absorptive form factors taken from the same source (except for the simulations in Section 4.3). Partial spatial and partial temporal coherence are neglected, no object tilt and no image spread are applied. The SrTiO₃ unit cell is divided into 2 sub slices along the [001] zone-axis, which is parallel to the electron beam direction, with a thickness of 0.195 nm each. Thermal vibrations at room temperature are considered by applying Debye–Waller damping to the elastic electron scattering potential with Debye parameters $B = 8\pi^2 \langle u^2 \rangle$ of $B(\text{Sr}) = 0.62 \text{ \AA}^2$, $B(\text{Ti}) = 0.44 \text{ \AA}^2$ and $B(\text{O}) = 0.71 \text{ \AA}^2$ in the projected plane of the SrTiO₃ structure [29], where $\langle u^2 \rangle$ denotes the mean squared atom displacement from the ideal geometric lattice site.

For the simulation of exit-plane wavefunctions in the EH studies, the phase gratings of the SrTiO₃ unit cell are sampled by 120×120 pixels. The resulting wavefunction is down-sampled to 40×40 pixels, yielding a sampling density of approximately 10 pm per pixel. An objective aperture is applied in reciprocal space in order to account for the effects of the reconstruction aperture in EH. The aperture radius is set to 25 mrad (12.7 nm^{-1}) and the defocus is set to zero, i.e., to the exit surface of the specimen.

For the simulation of FMSTEM data, a super cell of 4×4 unit cells of SrTiO₃ is simulated on a grid of 480×480 pixels. Hence, the corresponding diffraction patterns have sampling densities of 0.64 nm^{-1} per pixel in both x - and y -direction. This means that the largest spatial frequencies that carry information are approximately 100 nm^{-1} (200 mrad), when taking into account the anti-aliasing aperture used in the multislice simulation.

For comparability with the electron wavefunctions, the actual scan frame is set to 40×40 pixels per unit cell. In analogy to the objective aperture above, a semi-convergence angle of 25 mrad is used for all STEM calculations. Thus, the bright-field disks are sampled by approximately 40×40 pixels, as shown schematically for simulated diffraction patterns of different thicknesses in Fig. 1. The average lateral momentum transfer $\langle \vec{p} \rangle(\vec{r}_0)$ is then calculated from each diffraction pattern, including all scattering angles up to 200 mrad. The defocus is adjusted to give optimum contrast in the potential maps, i.e., the defocus at which the standard deviation of the image is largest. The value was obtained from simulated focus series.

The effect of TDS is included in simulations (in Section 4.3) by applying the frozen lattice approach [30], where the average over 800 (for thin objects) to 200 (for thick objects) “frozen lattice” configurations is performed for specimen thicknesses ranging from 0.4 nm up to 100 nm. The thermal vibrational amplitudes for the frozen lattice configurations are calculated from the Debye parameters mentioned

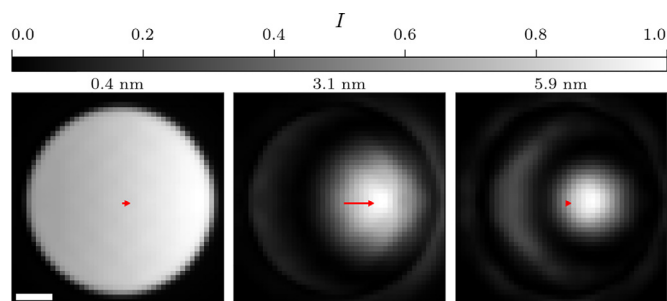


Fig. 1. Simulated diffraction patterns for three different thicknesses of SrTiO₃ displayed on arbitrary gray scales. The thicknesses are displayed above each image and the diffraction patterns are calculated in close proximity to the Sr column, as indicated by the white dot in Fig. 2c. The red arrows visualize the first moment vectors in each diffraction pattern. The scale bar is 5 nm⁻¹. (For interpretation of the references to color in this figure legend, the reader is referred to the web version of this article.)

above. The contribution to the diffraction patterns arising from purely elastic scattering is obtained by averaging the wavefunctions coherently in the back focal plane, whereas an incoherent average of the modulus squared of the wavefunctions yields the total scattering intensity [31]. The difference between the two is therefore the distribution of TDS in the diffraction pattern.

4. Results

The above derivations have demonstrated that a direct interpretation of EH and FMSTEM data in terms of electrical properties of the specimen relies on the phase approximation whose validity decreases with increasing specimen thickness. This is investigated in more detail now by interpreting the results of multislice simulations on the basis of the POA. The result is then compared with the ideal electrostatic potentials that both methods would yield if the POA holds, and the thickness-dependent (systematic?) error is quantified for EH and FMSTEM. To allow for a direct comparison, the electric fields obtained from FMSTEM are converted to the electrostatic potential by numerical integration as described in Appendix A.

4.1. Ideal electrostatic potentials

A fundamental difference between the potentials reconstructed from EH and FMSTEM stems from the convolution kernels, i.e., $B(\vec{r})$ and $B^2(\vec{r})$. In order to visualize this difference, the electrostatic potential of a single unit cell of SrTiO₃ was calculated by means of neutral atom scattering factors [28] including Debye-Waller factors. The potential was integrated along the [001] zone axis and divided by the specimen thickness t .

This potential is displayed in units of volt in the top row of Fig. 2, before and after convolution with the Fourier transformed apertures $B(\vec{r})$ and $B^2(\vec{r})$. These graphs represent the potentials that can ideally be obtained from a direct interpretation of the phase measured by EH (Fig. 2b), or the momentum transfer recorded by FMSTEM (Fig. 2c), respectively.

In the following, we will refer to these potentials as *ideal potentials* for the two techniques. Fig. 2d) schematically depicts the crystal structure of SrTiO₃ and a red square marks the projected unit cell, whereas e) shows line profiles extracted at the position of the white line shown in a). The convolution with $B(\vec{r})$ causes a dampening and point spread of the signal, which strongly broadens the peaks. In addition, a small peak between the Sr and O columns is introduced, which is a result of the oscillations of the Bessel function in $B(\vec{r})$. Although the point spread is less, the dampening effect is even stronger for $B^2(\vec{r})$, such that also the additional peak between the Sr and O columns disappears. This is a result of the sharper convolution kernel $B^2(\vec{r})$, which

is shown by a white dotted line in Fig. 2c).

Interestingly, the differences between EH and FMSTEM are already significant for a single oxygen atom, which is shown by the second peak in the line profile. The dampening of the reconstructed potential is much stronger in FMSTEM when compared to EH, but the point spread is stronger in EH. Hence, this could lead to an underestimation of the actual potential present in the specimen when interpreting experimental data. However, the characteristic shape of the potential is preserved better for a convolution with $B^2(\vec{r})$ rather than for $B(\vec{r})$.

The influence of these apertures is typically unavoidable when applying both techniques (even at optimum conditions), leading to fundamentally different results when reconstructing the electrostatic potentials in a straightforward manner from the phase of the electron wavefunction or from the first moment of diffraction patterns, respectively. Consequently, the same aperture function should not be confused with identical optical setups, as the application of these apertures acts differently on the contrast transfer in both techniques.

4.2. Dynamical diffraction

Apart from the convolution kernel, the most fundamental difference between the two techniques is given by the illumination, which is almost parallel in TEM (and EH) and convergent in STEM. As a result, dynamical diffraction effects are expected to be different for both techniques. In order to visualize the effects of dynamical diffraction, we have simulated electron wavefunctions and diffraction patterns for SrTiO₃ with specimen thicknesses ranging from a single layer (0.4 nm) up to 15 layers (5.9 nm), which is often still considered thin for conventional high-resolution TEM. From both data sets, we have reconstructed the projected electrostatic potential (c.f. Eqs. 8 & 16). Due to the integration of the STEM data, the mean inner potential is not retained in the FMSTEM potentials simulated here and it is set to match those of the potential calculated from neutral scattering factors.

For the STEM simulation, the defocus was chosen such that the contrast in the potential images is maximized, whereas the focus was set to the exit surface of the specimen for the simulation of electron wavefunctions.

If the probe is focused on the specimen entrance surface in STEM, i.e. $C_1 = 0$ nm, the signal will decrease rapidly with increasing specimen thickness, as shown in Fig. 3. Due to the high symmetry of the SrTiO₃, the unit cell is split here into two equal parts along the mirror plane crossing the Sr and Ti atoms, showing the optimum focus calculations in the upper right part and the zero-focus calculation in the lower left part of each image. It is obvious that the signal is almost lost when keeping the focus at $C_1 = 0$ nm, whereas at the optimum focus, the reconstructed potential is still clearly visible for all three thicknesses.

For the further comparison of EH and FMSTEM, we will always set the focus to the optimum value in STEM and to the exit-surface of the specimen in holography, i.e., $C_1 = 0$ nm. Whereas the defocus strongly affects the results in FMSTEM, in EH the defocus is mainly adjusted to minimize the phase noise in the reconstructed wavefunction [32]. After acquisition the defocus can be adjusted by multiplying a phase plate to the reconstructed electron wavefunction in reciprocal space [20,24,25].

Fig. 4 shows the direct comparison between the two techniques by means of reconstructed electrostatic potentials for various specimen thicknesses. The data calculated from simulated electron wavefunctions (EH) is shown in the lower left part of each image, whereas the STEM data is shown in the upper right part of each image.

It can be observed that at very low specimen thicknesses, the reconstructed potentials from both techniques are very similar, except for the more pronounced side maxima in interstitial regions for EH. However, with increasing thickness, the potentials calculated from electron wavefunctions reveal a blurring of the O peaks with decreasing peak values, whereas the Sr and Ti/O peaks become almost plateau-like. When increasing the thickness even further, beyond the range

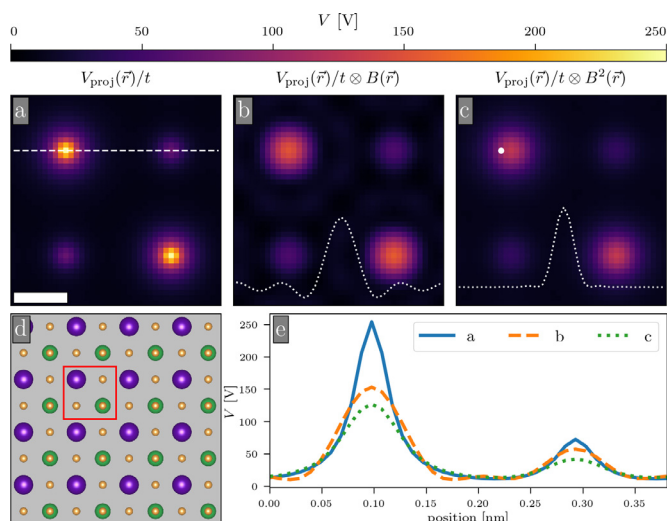


Fig. 2. Electrostatic potentials of a single unit cell of SrTiO₃ calculated from neutral scattering factors including Debye–Waller factors, integrated along the [001]-direction. a) shows the “sharp” atomic potential, whereas b) and c) show the potential convolved with Fourier transformed apertures $B(\vec{r})$ and $B^2(\vec{r})$ of radius 12.7 nm^{-1} , respectively. One-dimensional representations of the functions $B(\vec{r})$ and $B^2(\vec{r})$ are plotted as dotted white lines in the corresponding images. The SrTiO₃ crystal structure is schematically depicted in d), with a single unit cell marked by a red square. The colored spheres mark the atom positions, where Sr is purple, Ti is green, and O is orange. e) Line profiles of a)–c) extracted at the position of the white line shown in a). At the position of the white marker in c), diffraction patterns are calculated and displayed in Fig. 1. The scale bar is 0.1 nm. (For interpretation of the references to color in this figure legend, the reader is referred to the web version of this article.)

shown here, phase wrapping artifacts start to appear that make a reconstruction for the electrostatic potential more difficult. Depending on the sampling density, these phase wraps can be very difficult to unwrap reliably. We will thus focus our investigations on thin specimens.

In contrast to that, the potentials calculated from FMSTEM loose signal with increasing specimen thickness, despite using optimum focusing conditions. As a result, the peaks appear more blurry and dampened compared to the potentials obtained from EH. The different response to specimen thickness for both techniques can be attributed to the different illumination schemes and the corresponding electron diffraction and propagation inside the specimen. This is observed even better when comparing these reconstructed potentials (Fig 4) with their *ideal* counterpart (Fig. 2) introduced above. The differences between the simulated and *ideal* potentials are displayed in the insets of Fig. 5 for several specimen thicknesses.

Here, the lower left part of each image shows the difference between the electrostatic potentials obtained from simulated electron wavefunctions, as shown in Fig. 4 and the ideal potential calculated from neutral atom scattering factors shown in Fig. 2b. Similarly, the upper right part of each image shows the differences of potentials obtained from simulated diffraction patterns and the potential shown in Fig. 2c. The difference images appear overall more colorless (smaller difference to *ideal* potentials) in the upper right part of each image (FMSTEM data).

At very thin specimen thicknesses the differences are extremely small for both techniques, but it is observed that with increasing thickness, the different illumination settings and the corresponding electron diffraction inside the specimen lead to different results in the reconstructed electrostatic potentials. With increasing specimen thickness diffraction becomes more dynamical rather than kinematic and the deviation from the *ideal* potentials grows. In most cases the differences are strongest at the atomic positions and weakest in between. Overall, both data underestimate the potentials at the center of the atomic

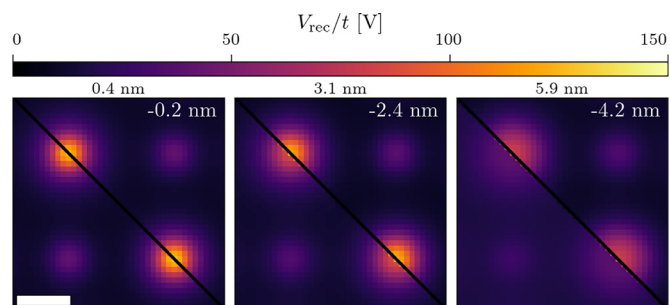


Fig. 3. Electrostatic potentials V_{rec}/t calculated from FMSTEM data with the focus value chosen to maximize the contrast in the potential images (upper right part of each image) and the focus set to the entrance surface of the specimen (lower left part of each image). The optimal defocus value is labeled in the upper right corner of each image (here a negative defocus value refers to the probe being focused below the entrance surface of the specimen). The specimen thickness is displayed above each image. The scale bar is 0.1 nm.

columns, when compared to the *ideal* potentials.

In order to present the quality of a direct interpretation of each technique as a function of thickness in a compact manner, we calculate the root mean square (RMS) deviation in a unit cell, according to the expression

$$\sigma_V = \sqrt{\frac{1}{N_x N_y} \sum_{x=0}^{N_x} \sum_{y=0}^{N_y} (V(x, y) - V_{\text{ref}}(x, y))^2}, \quad (17)$$

where $V(x, y)$ and $V_{\text{ref}}(x, y)$ denote the electrostatic potentials at position (x, y) obtained from simulation and neutral scattering factors, respectively. N_x and N_y are the numbers of pixels along the x and y direction. Although this quantity may not be the ideal measure in any scenario, it does allow for a simple and intuitive interpretation of the complex structures observed in the difference images. In particular, the RMS deviation is not capable of detecting strong relative changes with a comparably weak absolute value. The RMS deviation is displayed as a function of specimen thickness in Fig. 5.

Here, the blue lines corresponds to the EH data. As can be seen, the exclusion of the mean phase ϕ_0 of the wavefunction (dashed line), which is often associated with the mean inner potential under kinematic diffraction conditions [33–35], does not affect the RMS deviation significantly. The good match between the reconstructed and *ideal* potentials at very low thicknesses (at approximately 1 nm) confirms the validity of approximating the convolution in $V_{\text{rec}}^{\text{EH}}(\vec{r}) = V_{\text{proj}}(\vec{r}) \otimes B(\vec{r})$, as introduced in Eq. (8). The most interesting observation in Fig. 5 is the linear increase of the RMS deviation with specimen thickness. This demonstrates that, when imaging a specimen in zone-axis orientation, the simple and intuitive interpretation of the phase of the electron wavefunction in terms of an electrostatic potential is almost never fulfilled. Even for still very thin samples, e.g. 2–3 nm, the RMS deviation already takes values of about 3–4 V, which is approximately equivalent to the range of experimental phase noise in recent experiments [20]. Hence, there is a monotonic transition from a close-to-kinematic regime at the thinnest specimen thickness to a more dynamical regime at thicker specimens. This strong increase of dynamical diffraction effects are expected to be even more pronounced at lower primary electron energies, which are often applied in order to investigate beam-sensitive materials. The RMS deviation for the holographic data can be slightly optimized by adjusting the focus value, e.g. by maximizing the contrast in the phase image, which will move the RMS deviation by approximately 0.5–1 V down, as shown by the blue dotted curve. In order to set the displayed values of the RMS deviation in a more intuitive context, we calculated the RMS values of the *ideal* reference potentials shown in Fig. 2, which are 25 V for EH and 19 V for FMSTEM. Hence, an evaluation of the RMS deviation relative to the RMS of the corresponding potentials would bring the curves of EH and

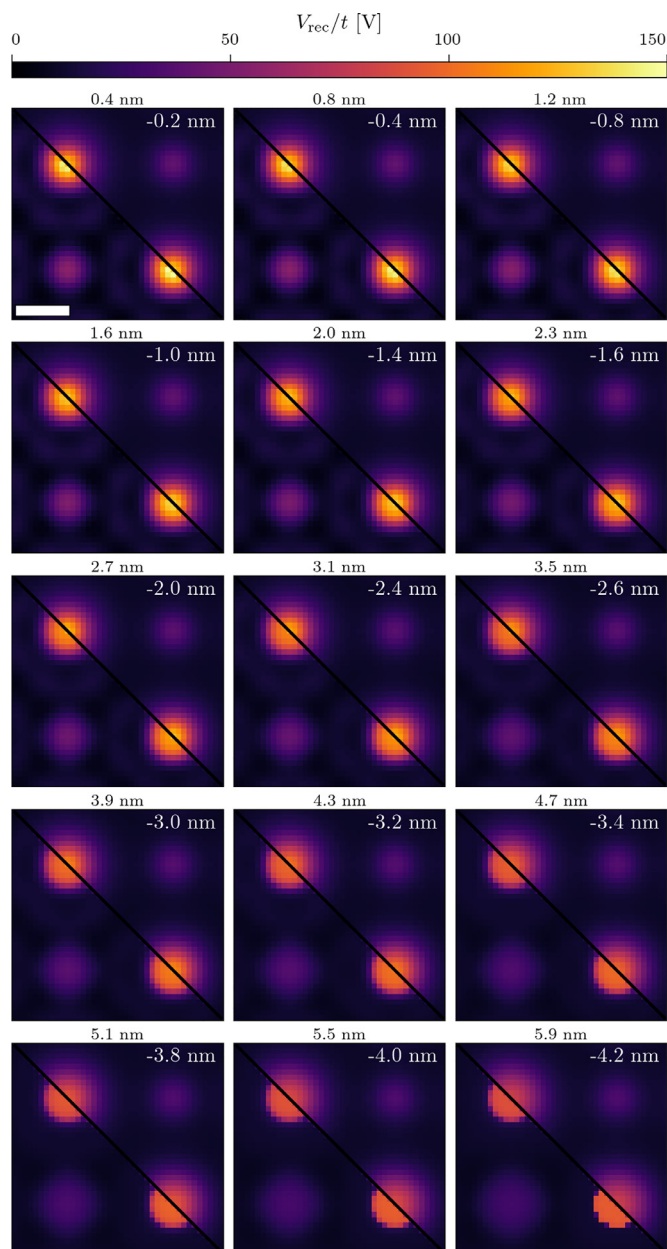


Fig. 4. Electrostatic potentials V_{rec}/t calculated from simulated electron wavefunctions (lower left part of each image) and calculated from FMSTEM data (upper right part of each image). The defocus value used for the STEM data is labeled in the upper right corner of each image. The specimen thickness was varied from 0.4 nm to 5.9 nm as displayed above each image. The scale bar is 0.1 nm.

FMSTEM closer together as the RMS of the *ideal* potential for EH is larger than the one for FMSTEM.

The green curve displays the RMS deviation obtained from the FMSTEM data, with the probe focused on the entrance surface ($C_1 = 0$ nm). In comparison to the EH data, the differences are measurably smaller up to a thickness of approximately 2 nm. Then the POA starts to break down for these settings and a similar value of the RMS deviation (for EH and FMSTEM) is reached at a thickness of approximately 3 nm. Due to a non-linear increase in RMS deviation, the deviation to the ideal potentials beyond this thickness is even greater than for the EH data. This emphasizes the importance of adjusting the focus carefully in FMSTEM experiments, at least for a certain regime of specimen thickness, which approximately includes all thicknesses above 2 nm in the present example.

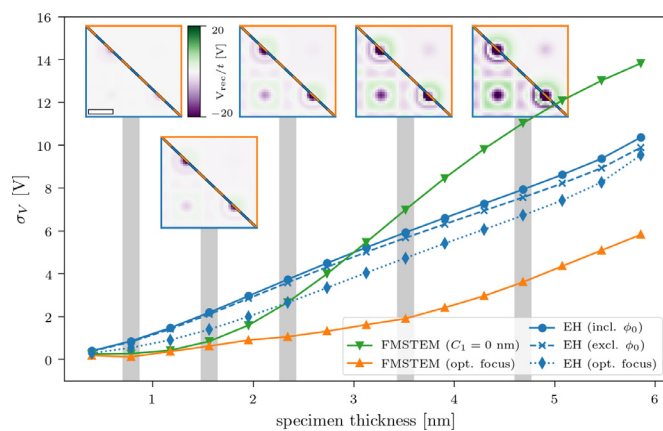


Fig. 5. RMS deviation between projected electrostatic potentials obtained from simulations of electron wavefunctions (EH) with different focus settings, including and excluding the contributions from the mean phase ϕ_0 , and FMSTEM with different focus settings and the *ideal* potentials calculated from neutral atomic scattering factors, plotted as a function of specimen thickness. At several specimen thicknesses, the difference images are shown in the insets. The scale bar in these images is 0.1 nm.

The situation changes drastically at optimum focusing conditions, which is displayed by the orange curve. The RMS is significantly lower compared to both the holographic data and the zero-focus FMSTEM data, except below 1.5 nm, where the zero-focus FMSTEM data yields comparable values of σ_v . At a specimen thickness of 6 nm the RMS deviation of the FMSTEM data (with optimum focus) is approximately equal to the RMS of the EH at just above 3 nm. The significantly lower values of σ_v for the FMSTEM data (with optimum focus) may be interpreted as a reduction of dynamical diffraction compared to EH, which is most likely a result of the different illumination settings in both techniques. For the convergent illumination in STEM, there are always incident waves that enter the specimen under angles that are slightly off zone-axis, such that the corresponding diffraction can be regarded more kinematic compared to waves that are in zone-axis. Hence, there are always kinematic contributions in the diffraction pattern. In the present example, the optimum foci are always located close to the exit-surface of the specimen. This implies that information of (almost) the full sample is transferred to the diffraction patterns at these focus settings, whereas only information of the upper parts of the specimen is transferred when the focus is set close to the entrance surface.

4.3. Thermal diffuse scattering

Thermal diffuse scattering (TDS) is a phenomenon that is well known in electron diffraction. As a result of a finite thermal energy, the atoms in the specimen are vibrating around their equilibrium position. Because the ideal lattice periodicity is disturbed, the scattering intensity from an incident electron probe is redistributed between the coherent Bragg reflections. The amount of thermal scattering typically grows with increasing specimen thickness and dominates over the Bragg contribution at high scattering angles. It is therefore a major contribution to the high-angle annular dark-field (HAADF) signal, which records only electrons that are scattered to high angles, e.g., from 40 mrad on. In contrast, it usually plays a minor role in coherent TEM or off-axis electron holography. In the latter, TDS only causes a change in the background intensity of the hologram, which is reflected by a dampening of the amplitude of the reconstructed wavefunction (that is typically only relevant for spatial resolutions that approach the atomic level), whereas the phase of the wavefunction remains unchanged [36].

A separation of the contributions from TDS and elastic (coherent) scattering is in the following achieved by simulations using the frozen

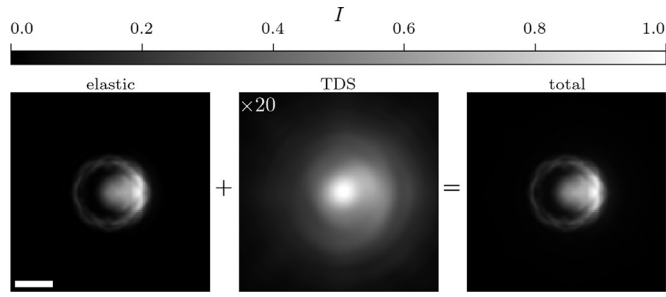


Fig. 6. Diffraction patterns for a 5.5 nm thick SrTiO₃ crystal, simulated using the frozen lattice approach. The diffraction patterns are calculated in close proximity to the Sr column, as indicated by the white circle in Fig. 2c. The intensity of the TDS pattern is enhanced by a factor of 20 for better visibility. The scale bar is 15 nm⁻¹.

lattice approach [30], where small atomic displacements are regarded stationary for each incoming electron. Various different configurations are then summed up in the detector plane. Performing an incoherent averaging of all individual intensity distributions yields the total scattering intensity. In contrast, the elastic scattering intensity is calculated by averaging the exit-plane wavefunctions coherently in the detector plane before calculating the modulus squared. The difference between the total and elastic intensities is then attributed to TDS [31], as shown exemplary for the corresponding diffraction patterns of 5.5 nm thick SrTiO₃ in Fig. 6. As for the previous investigations, the focus in the STEM simulations is optimized to maximize the contrast in the potential images. Interestingly, the TDS diffraction is not radially symmetric. Hence, depending on the probe position, such an asymmetric intensity distribution could in principle noticeably affect the first moment of the diffraction pattern, as the TDS intensities are typically located at high scattering angles.

Before investigating the influence of TDS on the average momentum transfer $\langle \vec{p} \rangle$, we calculate the contribution of TDS compared to the total scattering intensity. The scattering intensity of TDS I_{TDS} is calculated from the sum of the TDS diffraction pattern divided by the sum of the total diffraction pattern and is plotted as a function of specimen thickness on a semi-logarithmic scale in Fig. 7. The solid line represents the unit cell average, whereas the dashed line shows the maximum intensity within each unit cell, which in the present example is always located at the Sr site, as shown in the insets. Whereas the unit cell averaged intensity shows a monotonic increase with specimen thickness, the maximum intensity shows a local peak at approximately 4 nm

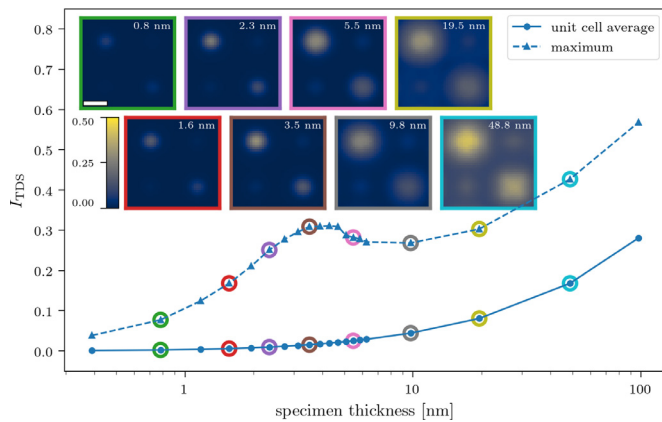


Fig. 7. Thermal diffuse scattering intensity I_{TDS} plotted as a function of specimen thickness on a semi-logarithmic scale. The solid line represents the unit cell average, whereas the dashed line shows the maximum intensity within each unit cell (typically located at the Sr site). Insets show the scattering intensity distribution in the unit cell for several thicknesses, as marked by the colored frames and circles. The scale bar is 0.1 nm.

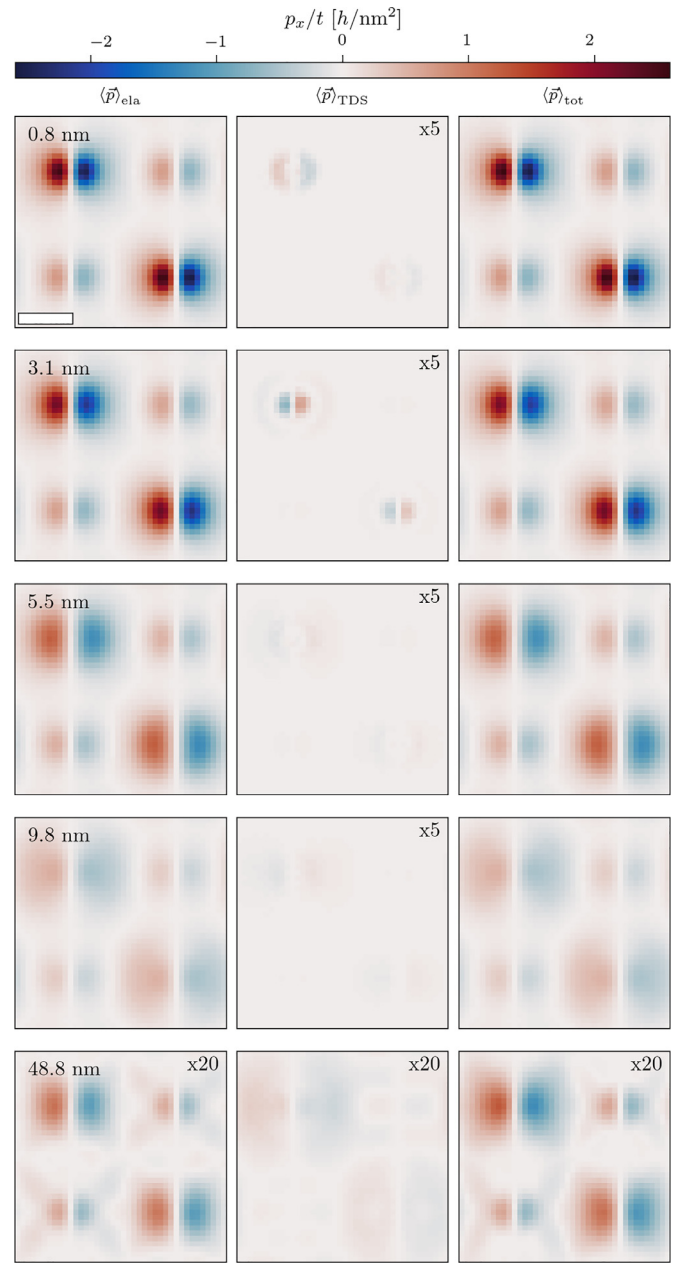


Fig. 8. x-component of momentum transfer (divided by specimen thickness t) simulated with the frozen lattice approach. Each row represents a different specimen thickness, as labeled in the top left corner of the first image in each row. The columns show from left to right the momentum transfer of the elastic, TDS and total scattering signal, as given by Eq. (18). All images are plotted on the same scale, except where a multiplication factor is indicated in the top right corner of the image. The scale bar is 0.1 nm.

with values of I_{TDS} of above 30 %. Thus, close to heavy atomic sites TDS may already have a significant effect on the momentum transfer at relatively thin specimens of only a few nm. In contrast, TDS is completely negligible in the vicinity of light atomic columns.

The average momentum transfers are calculated by means of the first moment from the diffraction patterns of the individual signal contributions, which yield

$$\langle \vec{p} \rangle_{\text{tot}} = h \frac{\sum_{\vec{k}} \vec{k} I_{\text{tot}}(\vec{k})}{\sum_{\vec{k}} I_{\text{tot}}(\vec{k})}, \quad \langle \vec{p} \rangle_{\text{ela}} = h \frac{\sum_{\vec{k}} \vec{k} I_{\text{ela}}(\vec{k})}{\sum_{\vec{k}} I_{\text{ela}}(\vec{k})}$$

and $\langle \vec{p} \rangle_{\text{TDS}} = \langle \vec{p} \rangle_{\text{tot}} - \langle \vec{p} \rangle_{\text{ela}}$, (18)

where h is the Planck constant. As in the previous section, the first moments are calculated including all contributions up to a scattering angle of 200 mrad and calculations are performed in optimum focus conditions, i.e. maximal contrast in potential images. The total momentum transfer $\langle \vec{p} \rangle_{\text{tot}}$ represents the quantity that is measured from diffraction patterns that contain both elastically and thermal diffuse scattered electrons, such as in a conventional FMSTEM experiment. Its x -component is displayed for several thicknesses in the third column of Fig. 8. All momentum transfers in this figure are divided by the specimen thickness t , in order to display them on the same color scale. As observed in the previous section, the signal of $\langle \vec{p} \rangle_{\text{tot}}/t$ drops to smaller values with an increasing specimen thickness.

In order to record only elastically scattered electrons, which would yield the momentum transfer $\langle \vec{p} \rangle_{\text{ela}}$ as given in Eq. (18), TDS needs to be suppressed. In practice, this is difficult to achieve. Although TDS is reduced by cooling of the specimen (to liquid helium temperature), this also changes the potential of the specimen that the electrons experience, i.e., the potential becomes much sharper at atomic positions, where dynamical diffraction effects can be strongly enhanced. Another option is given by applying an energy filter before recording the diffraction patterns. Thus, $\langle \vec{p} \rangle_{\text{ela}}$, which is shown in the first column of Fig. 8, represents the signal obtained from a diffraction pattern of “purely” elastically scattered electrons, similar to the signal obtained in EH.

The difference between this purely elastic and the total momentum transfer can then be understood as the error caused by TDS, as given by $\langle \vec{p} \rangle_{\text{TDS}}$ in Eq. (18) and displayed in the second column of Fig. 8. It is observed that the momentum transfers of $\langle \vec{p} \rangle_{\text{tot}}$ and $\langle \vec{p} \rangle_{\text{ela}}$ are actually extremely similar for thin specimens ($t < 10$ nm). Interestingly, the momentum transfer is reversed at a specimen thickness of approximately 3 nm, which is observed clearly at the Sr and Ti columns. Here, the momentum transfer is negative at the left side of the columns, whereas it is positive in the elastic signal. However, as the magnitudes of $\langle \vec{p} \rangle_{\text{TDS}}$ are significantly smaller than $\langle \vec{p} \rangle_{\text{ela}}$, this effect is negligible. When increasing the specimen thickness, the error due to TDS increases, which causes the total momentum transfer to deviate more strongly from the elastic signal. However, at 50 nm the elastic momentum transfer is still stronger than the one obtained from TDS.

In order to quantify the effect of TDS, we calculate the RMS of the corresponding momentum transfers, which we denote as σ_p in the following. Fig. 9 shows the RMS of the momentum transfers associated with TDS for different cutoff angles ranging from 30 mrad to 200 mrad plotted against specimen thickness on a double logarithmic scale. In addition, the RMS of the elastic signal is displayed by a dashed black line. The different cutoff angles are important parameters, as

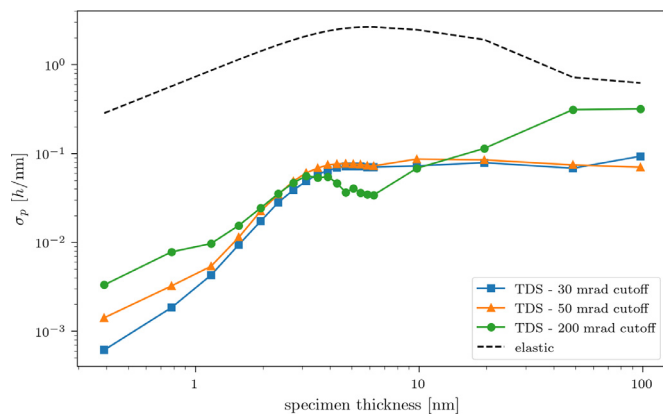


Fig. 9. RMS of the momentum transfers σ_p associated with TDS (colored lines) for different cutoff frequencies plotted against specimen thickness on a double logarithmic scale. The dashed black line presents the RMS of the elastic momentum transfer.

experimental data is often limited to a certain angular range, depending on the position and size of the detector, as well as the camera length.

The first observation from Fig. 9 is that σ_p of the elastic signal is at least one order of magnitude larger than for the TDS contributions up to a thickness of approximately 20 nm. For thicker specimens, the RMS of the elastic signal and the TDS signal (including scattering angles up to 200 mrad) approach each other, but the elastic part is still stronger even at a thickness of 100 nm. Obviously, the RMS of the TDS signals are smallest for the thinnest specimens. Interestingly, a small peak is observed at approximately 3–4 nm for the green curve (TDS with 200 mrad cutoff), which is at the same position as the peak of the maximum TDS scattering intensity in Fig. 7. This peak is not observed for the smaller cutoff angles of 30 and 50 mrad. For these angles, σ_p remains much smaller for thicker specimens (above 20 nm), when compared to the RMS of the elastic signal.

Hence, we can conclude that, although TDS significantly contributes to the diffraction patterns especially at high angles, the effect on the momentum transfer is relatively small when compared to purely elastic scattering, as long as the specimen is thin enough (below 20 nm in the current example). For thicker specimens the effects TDS can become non-negligible. However, a limitation of the spatial frequency cutoff to about twice the semi-convergence angle already reduces the TDS “error” dramatically even for thicker specimens of approximately 100 nm. This is of importance, as in a real experiment, the physical size of contemporary electron detectors is finite and the camera length in the microscope is limited, which in turn also limits the maximal scattering detection angle.

5. Discussion

5.1. Simulation results

It was shown above that electrostatic potentials reconstructed from EH and FMSTEM data are fundamentally different, which is a result of the probe-forming / objective aperture and the fact that FMSTEM works on an intensity level, whereas EH works with coherent wavefunctions. This also allows to adjust coherent aberrations, such as defocus, after acquisition in EH, whereas the defocus strongly affects the reconstructed potentials in FMSTEM. However, in optimum focusing conditions, the interaction with the specimen is more kinematic and the signal is in better agreement to simulations up to larger thicknesses, when compared to EH. It was also shown that TDS plays a minor role in FMSTEM, as long as the sample is thin enough. For thicker specimens it can lead to significant deviations of the measured signal from the expectations. In contrast, TDS does not affect the phase of the reconstructed wavefunction in EH. Instead, it only dampens the amplitude contrast and reduces the signal-to-noise ratio in the wavefunction, as it reduces the number of coherently scattered electrons contributing to the sideband.

5.2. Further aspects

Whereas the preceding section attempted an in-depth quantitative analysis of factors distinguishing EH and FMSTEM from the fundamental physics point of view, we briefly address further aspects that will affect a comparison of the two approaches in practice. The goal is to lay a qualitative basis for a comparative study that focuses on practical aspects and links performance limits that are predominantly present in methodology-specific form [13,37–40].

Partial spatial coherence. In STEM, the recorded signal at each (nominal) scan position is actually formed by the incoherent summation of signals that are spatially distributed around the nominal scan position, which is usually described by a Lorentzian or Gaussian-shaped source distribution function. This leads to an attenuation of fine details in the diffraction pattern [41]. For first moment imaging it was shown that partial spatial coherence can be taken into account by a cross-

correlation of the (coherent) vector field $\langle \vec{p} \rangle$ with the source spread of the electron source [14]. In electron holography, partial spatial coherence causes an illumination of the specimen with plane waves having an angular spread, and the resulting holograms have to be summed incoherently. For sufficiently high coherence, which is usually present nowadays, partial spatial coherence essentially affects the interference fringe contrast and therefore the signal-to-noise ratio in the reconstructed wavefunction. This can be accounted for by the convolution of the exit-plane wavefunction with an envelope function that depends primarily on the source spread.

Partial temporal coherence. In STEM, the energy spread of the cathode as well as fluctuations of the high tension, the probe-forming lens current and its chromatic aberration cause an attenuation of contrast. In the FMSTEM case, this can be taken into account by a weighted sum over $\langle \vec{p} \rangle$ present for different foci, with the focal spread parameter describing the width of the distribution of effective foci present in the STEM probe. To obtain partially (temporal) coherent diffraction patterns, however, individual diffraction patterns for each focus must be summed incoherently with proper weighting. Recent studies have stressed the importance of partial temporal coherence in STEM especially of thin specimen [42–44]. Up to now, no probe-forming system with chromatic aberration correction exists whereas chromatic aberration correctors have entered the imaging system of conventional TEMs. In EH, an envelope function defined by the focal spread parameter must be convolved with the exit-plane wavefunction, leading to a dampening of high spatial frequencies as well.

Instabilities. Mechanical as well as electrical instabilities and thermal magnetic field noise [45] deteriorate the image quality in both EH and STEM. The comparably long recording times of several seconds in EH provide a time-averaged wavefunction that suffered an attenuation of high spatial frequencies. In STEM, some sources of instability can be taken into account by the source spread parameter [45], leading to a similar effect. However, the sequential nature of data acquisition at kHz to MHz rates causes severe deviations of the scan position from their regular scan raster (scan noise) due to, e.g., stray fields acting on the deflection coils in STEM. In addition, specimen drift distorts the image of the atomic lattice, rather than blurring it. These effects must be considered when, e.g., integrating or differentiating $\langle \vec{p} \rangle$ to obtain the electrostatic potential or the charge density, respectively. Commonly scan noise is ignored or STEM data is corrected for by non-rigid registration schemes applied to time series of STEM images [46,47]. However, no technique is available yet which can reconstruct the true scan positions from STEM data affected by scan noise and scan distortions.

Dose efficiency and noise. The question how precisely the atomic-scale electrical properties can be measured by MRSTEM, FMSTEM or electron holography with a given dose is not straightforward to answer as to a conceptual comparison. Especially for the investigation of beam sensitive materials, the dose efficiency will be a key characteristic for the phase retrieval method of choice. Whether the number of electrons (hitting the specimen) required to achieve a comparable signal resolution is larger in FMSTEM or EH is unclear so far. However, in real experiments, this number depends strongly on the experimental conditions, i.e., the detector properties, apertures, camera length, etc. For the phase contrast STEM techniques, no comprehensive analytical treatment of the propagation of Poissonian noise appears available so far. In electron holography, the phase detection limit is proportional to the reciprocal fringe contrast and the reciprocal square root of the number of electrons [37]. A more detailed analytical treatment was suggested recently [48]. In FMSTEM the noise of each scan pixel is independent of all other pixels for the first moment determination. For the calculation of the charge density or potential differences, nearest neighbour pixel contribute, too. However, Fourier transforms involved in electron holography orptychography, combined with the application of masks, can lead to correlated noise to be considered carefully for the analysis of precision and accuracy.

Versatility. Energy-dispersive X-ray analysis, secondary electron detection, cathodoluminescence and Z-contrast imaging can readily be combined with MRSTEM and FMSTEM so as to obtain chemical, topological and optical information at a spatial resolution down to the atomic scale. EH can be combined with these techniques as well, yielding, however, only averaged information about the interaction volume. Nevertheless EH is the only technique that allows for a quasi-direct reconstruction of the whole wavefunction in the image plane, which allows for a correction of coherent aberrations post-acquisition. In addition, a conventional HRTEM is available from the centerband of the hologram. For FMSTEM, a-posteriori aberration correction has not been reported so far. Instead, bright and dark field images are available, providing the scattering cross sections for certain solid angles. If calculated from MRSTEM data rather than recorded directly using position-sensitive detectors [49], high flexibility is available to apply virtual detectors covering dedicated solid angles, or to perform custom calculations, e.g., higher order moments.

Detection, sampling and signal processing. High detector speed is a key component for MRSTEM, currently allowing for dwell times in the ms-range and slightly below [7–10]. Typical scan frame widths therefore do not exceed several hundreds of pixels, whereas conventional STEM dwell times and scan frame widths of thousands of pixels can be achieved with novel position-sensitive devices for FMSTEM which are capable of μ s-range dwell times [49]. Electron hologram recording, in contrast, relies primarily on camera quality in terms of the modulation transfer function (MTF) and a preferably large pixel array. The MTF of conventional charge-coupled devices (CCDs) at the Nyquist frequency can be below 10 %, whereas novel direct electron counting modes in CMOS cameras provide values above 60 % [50]. Similarly, a blurring of the recorded diffraction patterns is observed in MRSTEM [51,52].

Note that the single sideband reconstruction scheme also limits the number of (meaningful) pixels in the reconstructed wavefunction. The number of real-space pixels in MRSTEM/FMSTEM and EH is thus comparable. However, increasing the real space sample size and, with it, the field of view or the sampling frequency, appears technologically more straightforward in STEM than in electron holography, in which the field of view (of the reconstructed wavefunction) is limited by the interference width of the hologram. Moreover, increasing the number of scan pixels by driving the scan coils is much more straightforward technologically than increasing the pixel array size of cameras.

Finally, off-axis electron holography inherently requires a known reference wave, for which a vacuum region is usually used. Besides the fact that this limits the analysis to specimen edges, this reference wave might be perturbed in an unknown manner, e.g., by electromagnetic stray fields. Although MRSTEM and FMSTEM are not restricted to specimen edges and no vacuum reference is needed, quantitative work should measure, e.g., first moments, relative to a reference scan without specimen. Whereas this compensates for a movement of the diffraction pattern as a function of the scan position, electromagnetic stray fields might be different from the actual recording with specimen, which can introduce similar artefacts as the perturbed reference wave phenomenon in electron holography. In addition, when reconstructing the electron wavefunction from a hologram of a slightly thicker specimen at very high spatial resolution phase wraps can appear, which may be very difficult or impossible to unwrap.

6. Conclusion

Off-axis electron holography and first moment STEM are among the most popular techniques applied in TEM in order to measure electromagnetic properties with high spatial resolution. In this work, we have outlined the fundamental differences between these two techniques by analyzing electrostatic potentials directly reconstructed from simulated data sets. One fundamental difference is the convolution kernel, which results from the reconstruction/objective aperture in EH and the probe-

forming aperture in STEM. As a result of the different illumination schemes, i.e. parallel for EH and convergent for STEM, dynamical diffraction is less severe in FMSTEM, when investigating a sample in zone-axis orientation (at optimum focusing conditions). We showed that the focus plays an important role in FMSTEM, as the signal strongly degrades with increasing specimen thickness, if the electron probe is focused on the entrance surface of the specimen. Instead, when adjusting the focus to maximize the contrast in the electrostatic potential image, the signal is preserved significantly better with increasing specimen thickness. In addition, we have shown that TDS only affects the first moment (in the vicinity of heavy atoms) if the specimen is relatively thick (approximately above 20 nm for SrTiO₃ imaged at 300 kV), whereas in EH the phase remains unchanged, as inelastically scattered electrons are not contributing to the coherent sideband. However, inelastic scattering reduces the number of electrons in the sideband and therefore also the hologram fringe contrast and the resulting signal-to-noise ratio in the reconstructed electron wavefunction.

Last but not least, we outlined further aspects that (may) affect the results when recording real experimental data. Effects, such as partial temporal and spatial coherence, instabilities of any kind or the detector properties are important parameters in such experiments. Although, some of these effects may represent experimental challenges at the moment, there can also be great benefits when using these techniques,

Appendix A. Integration by means of Fourier transforms

Let $f(\vec{r})$ be a continuously differentiable function, whose derivative is written as $f'(\vec{r}) = \vec{\nabla}f(\vec{r})$. Using the definition $\mathcal{F}[f'(x)] = 2\pi ik\mathcal{F}[f(x)]$ from above, we can obtain the function $f(\vec{r})$ from its derivative, according to the expression

$$\mathcal{F}[f'(\vec{r})] = \mathcal{F}[f(\vec{r})]2\pi ik \quad (\text{A.1})$$

$$\vec{k}\mathcal{F}[f'(\vec{r})] = \mathcal{F}[f(\vec{r})]2\pi ik^2, \quad (\text{A.2})$$

where $k = \left| \vec{k} \right|^2$. In the last step, both sides have been multiplied by \vec{k} . Hence, we can rewrite Eq. (A.2) as

$$\mathcal{F}[f(\vec{r})] = \vec{k}\mathcal{F}[f'(\vec{r})] \frac{1}{2\pi ik^2}, \quad (\text{A.3})$$

which transforms to the following expression when taking an inverse Fourier transform

$$f(\vec{r}) = \mathcal{F}^{-1} \left[\vec{k}\mathcal{F}[f'(\vec{r})] \frac{1}{2\pi ik^2} \right]. \quad (\text{A.4})$$

It should be noted that Eq. (A.4) is not defined for $k = 0$, which is the equivalent for the unknown integration constant, i.e., the mean of the function $f(\vec{r})$ after integration is not necessarily correct.

References

- [1] D. Gabor, A new microscopic principle, *Nature* 161 (1948) 777–778.
- [2] G. Möllenstedt, H. Wahl, Elektronenholographie und Rekonstruktion mit Laserlicht, *Naturwissenschaften* 55 (1968) 340–341.
- [3] W.D. Rau, P. Schwander, F.H. Baumann, W. Höppner, A. Ourmazd, Two-dimensional mapping of the electrostatic potential in transistors by electron holography, *Phys. Rev. Lett.* 82 (12) (1999) 2614–2617.
- [4] M.A. Gribelyuk, M.R. McCartney, J. Li, C.S. Murthy, P. Ronsheim, B. Doris, J.S. McMurray, S. Hegde, D.J. Smith, Mapping of electrostatic potential in deep submicron CMOS devices by electron holography, *Phys. Rev. Lett.* 89 (2) (2002) 25502.
- [5] A.C. Twitchett-Harrison, T.J.V. Yates, R.E. Dunin-Borkowski, P.A. Midgley, Quantitative electron holographic tomography for the 3D characterisation of semiconductor device structures, *Ultramicroscopy* 108 (11) (2008) 1401–1407.
- [6] A. Marchewka, D. Cooper, C. Lenser, S. Menzel, H. Du, R. Dittmann, R.E. Dunin-Borkowski, R. Waser, Determination of the electrostatic potential distribution in Pt/Fe:SrTiO₃/Nb:SrTiO₃ thin-film structures by electron holography, *Sci. Rep.* 4 (2014) 6975.
- [7] K. Müller-Caspary, A. Oelsner, P. Potapov, Two-dimensional strain mapping in semiconductors by nano-beam electron diffraction employing a delay-line detector, *Appl. Phys. Lett.* 107 (7) (2015) 072110.
- [8] K. Müller, H. Ryll, I. Ordavo, S. Ihle, L. Strüder, K. Volz, J. Zweck, H. Soltau, A. Rosenauer, Scanning transmission electron microscopy strain measurement from millisecond frames of a direct electron charge coupled device, *Appl. Phys. Lett.* 101 (21) (2012) 212110.
- [9] H. Ryll, M. Simson, R. Hartmann, P. Holl, M. Huth, S. Ihle, Y. Kondo, P. Kotula, A. Liebel, K. Müller-Caspary, A. Rosenauer, R. Sagawa, J. Schmidt, H. Soltau, L. Strüder, A pnCCD-based, fast direct single electron imaging camera for TEM and STEM, *J. Instrum.* 11 (04) (2016) P04006.
- [10] R. Plackett, I. Horswell, E.N. Gimenez, J. Marchal, D. Omar, N. Tartoni, Merlin: a fast versatile readout system for Medipix3, *J. Instrument.* 8 (2013) C01038.
- [11] M.W. Tate, P. Purohit, D. Chamberlain, K.X. Nguyen, R. Hovden, C.S. Chang, P. Deb, E. Turgut, J.T. Heron, D.G. Schlom, D.C. Ralph, G.D. Fuchs, K.S. Shanks, H.T. Philipp, D.A. Muller, S.M. Gruner, High dynamic range pixel array detector for scanning transmission electron microscopy, *Microsc. Microanal.* 22 (2016) 237–249.
- [12] K. Müller, F.F. Krause, A. Béch e, M. Schowalter, V. Galioit, S. Löffler, J. Verbeeck, J. Zweck, P. Schattschneider, A. Rosenauer, Atomic electric fields revealed by a quantum mechanical approach to electron picodiffraction, *Nat. Commun.* 5 (2014) 5653.
- [13] K. Müller-Caspary, F.F. Krause, T. Grieb, S. Löffler, M. Schowalter, A. Béch e, V. Galioit, D. Marquardt, J. Zweck, P. Schattschneider, J. Verbeeck, A. Rosenauer, Measurement of atomic electric fields and charge densities from average momentum transfers using scanning transmission electron microscopy, *Ultramicroscopy* 178 (2017) 62–80.
- [14] K. Müller-Caspary, M. Duchamp, M. Rösner, V. Migunov, F. Winkler, H. Yang, M. Huth, R. Ritz, M. Simson, S. Ihle, H. Soltau, T. Wehling, R.E. Dunin-Borkowski, S. Van Aert, A. Rosenauer, Atomic-scale quantification of charge densities in two-dimensional materials, *Phys. Rev. B* 98 (12) (2018) 121408.
- [15] F. Hüe, J.M. Rodenburg, A.M. Maiden, F. Sweeney, P.A. Midgley, Wave-front phase retrieval in transmission electron microscopy via Ptychography, *Phys. Rev. B* 82 (12) (2010) 121415.

- [16] P.D. Nellist, J.M. Rodenburg, Electron ptychography. I. experimental demonstration beyond the conventional resolution limits, *Acta Crystallographica Section A* 54 (1) (1998) 49–60.
- [17] J.M. Rodenburg, Ptychography and related diffractive imaging methods, in: Hawkes (Ed.), *Advances in Imaging and Electron Physics*, 150 Elsevier, 2008, pp. 87–184.
- [18] D. Typke, D. Köstler, Determination of the wave aberration of electron lenses from superposition diffractograms of images with differently tilted illumination, *Ultramicroscopy* 2 (1976) 285–295.
- [19] M. Linck, B. Freitag, S. Kujawa, M. Lehmann, T. Niermann, State of the art in atomic resolution off-axis electron holography, *Ultramicroscopy* 116 (2012) 13–23.
- [20] F. Winkler, J. Barthel, A.H. Tavabi, S. Borghardt, B.E. Kardynal, R.E. Dunin-Borkowski, Absolute scale quantitative off-axis electron holography at atomic resolution, *Phys. Rev. Lett.* 120 (15) (2018) 156101.
- [21] C. Ophus, H.I. Rasool, M. Linck, A. Zettl, J. Giston, Automatic software correction of residual aberrations in reconstructed HRTEM exit waves of crystalline samples, *Adv. Struct. Chem. Imaging* 2 (1) (2017) 15.
- [22] D. Stenkamp, Detection and quantitative assessment of image aberrations from single HRTEM lattice images, *J. Microscopy* 190 (1–2) (1998) 194–203.
- [23] D. Tang, H.W. Zandbergen, J. Jansen, M. Op de Beeck, D. Van Dyck, Fine-tuning of the focal residue in exit-wave reconstruction, *Ultramicroscopy* 64 (1) (1996) 265–276.
- [24] A. Thust, M.H.F. Overwijk, W.M.J. Coene, M. Lentzen, Numerical correction of lens aberrations in phase-retrieval HRTEM, *Ultramicroscopy* 64 (1) (1996) 249–264.
- [25] M. Lehmann, Determination and correction of the coherent wave aberration from a single off-axis electron hologram by means of a genetic algorithm, *Ultramicroscopy* 85 (3) (2000) 165–182.
- [26] J.M. Cowley, A.F. Moodie, The scattering of electrons by atoms and crystals. i. a new theoretical approach, *Acta Crystallographica* 10 (10) (1957) 609–619.
- [27] J. Barthel, Dr. probe: a software for high-resolution STEM image simulation, *Ultramicroscopy* 193 (2018) 1–11.
- [28] A. Weickenmeier, H. Kohl, Computation of absorptive form factors for high-energy electron diffraction, *Acta Crystallographica Section A* 47 (5) (1991) 590–597.
- [29] Y.A. Abramov, V.G. Tsirelson, V.E. Zavadnik, S.A. Ivanov, I.D. Brown, The chemical bond and atomic displacements in SrTiO₃ from X-ray diffraction analysis, *Acta Cryst. B* 51 (6) (1995) 942–951.
- [30] P. Xu, R.F. Loane, J. Silcox, Energy-filtered convergent-beam electron diffraction in STEM, *Ultramicroscopy* 38 (2) (1991) 127–133.
- [31] B.D. Forbes, A.V. Martin, S.D. Findlay, A.J. D'Alfonso, L.J. Allen, Quantum mechanical model for phonon excitation in electron diffraction and imaging using a Born-Oppenheimer approximation, *Phys. Rev. B* 82 (10) (2010) 104103.
- [32] M. Linck, Optimum aberration coefficients for recording high-resolution off-axis holograms in a Cs-corrected TEM, *Ultramicroscopy* 124 (2013) 77–87.
- [33] F. Winkler, A.H. Tavabi, J. Barthel, M. Duchamp, E. Yucelen, S. Borghardt, B.E. Kardynal, R.E. Dunin-Borkowski, Quantitative measurement of mean inner potential and specimen thickness from high-resolution off-axis electron holograms of ultra-thin layered WSe₂, *Ultramicroscopy* 178 (2017) 38–47.
- [34] P. Kruse, M. Schowalter, D. Lamoen, A. Rosenauer, D. Gerthsen, Determination of the mean inner potential in III-V semiconductors, Si and Ge by density functional theory and electron holography, *Ultramicroscopy* 106 (2) (2006) 105–113.
- [35] M. Gajdardziska-Josifovska, M.R. McCartney, W.J. de Ruijter, D.J. Smith, J.K. Weiss, J.M. Zuo, Accurate measurements of mean inner potential of crystal wedges using digital electron holograms, *Ultramicroscopy* 50 (3) (1993) 285–299.
- [36] Z.L. Wang, Thermal diffuse scattering in high-resolution electron holography, *Ultramicroscopy* 52 (3) (1993) 504–511.
- [37] H. Lichte, Performance limits of electron holography, *Ultramicroscopy* 108 (3) (2008) 256–262.
- [38] J.P. Buban, Q. Ramasse, B. Gipson, N.D. Browning, H. Stahlberg, High-resolution low-dose scanning transmission electron microscopy, *J. Electron Microscopy* 59 (2) (2010) 103–112.
- [39] E. Yücelen, I. Lazić, E.G.T. Bosch, Phase contrast scanning transmission electron microscopy imaging of light and heavy atoms at the limit of contrast and resolution, *Sci. Rep.* 8 (1) (2018) 2676.
- [40] J. Fatermans, A.J. den Dekker, K. Müller-Caspary, I. Lobato, C.M. O'Leary, P.D. Nellist, S. Van Aert, Single atom detection from low contrast-to-noise ratio electron microscopy images, *Phys. Rev. Lett.* 121 (5) (2018) 56101.
- [41] C. Dwyer, R. Erni, J. Etheridge, Measurement of effective source distribution and its importance for quantitative interpretation of STEM images, *Ultramicroscopy* 110 (8) (2010) 952–957.
- [42] A. Beyer, J. Belz, N. Knaub, K. Jandieri, K. Volz, Influence of spatial and temporal coherences on atomic resolution high angle annular dark field imaging, *Ultramicroscopy* 169 (2016) 1–10.
- [43] K. Kuramochi, T. Yamazaki, Y. Kotaka, M. Ohtsuka, I. Hashimoto, K. Watanabe, Effect of chromatic aberration on atomic-resolved spherical aberration corrected STEM images, *Ultramicroscopy* 110 (1) (2009) 36–42.
- [44] A. Beyer, R. Straubinger, J. Belz, K. Volz, Local sample thickness determination via scanning transmission electron microscopy defocus series, *J. Microscopy* 262 (2) (2016) 171–177.
- [45] S. Uhlemann, H. Müller, P. Hartel, J. Zach, M. Haider, Thermal magnetic field noise limits resolution in transmission electron microscopy, *Phys. Rev. Lett.* 111 (4) (2013) 46101.
- [46] L. Jones, P.D. Nellist, Identifying and correcting scan noise and drift in the scanning transmission electron microscope, *Microscopy Microanal.* 19 (4) (2013) 1050–1060.
- [47] L. Jones, H. Yang, T.J. Pennycook, M.S.J. Marshall, S. Van Aert, N.D. Browning, M.R. Castell, P.D. Nellist, Smart Align a new tool for robust non-rigid registration of scanning microscope data, *Adv. Struct. Chem. Imaging* 1 (1) (2015) 8.
- [48] S. Chen, C. Li, C. Ma, T.-C. Poon, Y. Zhu, Phase sensitivity of off-axis digital holography, *Opt. Lett.* 43 (20) (2018) 4993–4996.
- [49] F. Schwarzhuber, P. Melzl, S. Pöllath, J. Zweck, Introducing a non-pixelated and fast centre of mass detector for differential phase contrast microscopy, *Ultramicroscopy* 192 (2018) 21–28.
- [50] S.L.Y. Chang, C. Dwyer, J. Barthel, C.B. Boothroyd, R.E. Dunin-Borkowski, Performance of a direct detection camera for off-axis electron holography, *Ultramicroscopy* 161 (2016) 90–97.
- [51] A. Lubk, J. Zweck, Differential phase contrast: an integral perspective, *Phys. Rev. A* 91 (2) (2015) 23805.
- [52] J.A. Mir, R. Clough, R. MacInnes, C. Gough, R. Plackett, I. Shipsey, H. Sawada, I. MacLaren, R. Ballabriga, D. Maneuski, V. O'Shea, D. McGrouther, A.I. Kirkland, Characterisation of the Medipix3 detector for 60 and 80 keV electrons, *Ultramicroscopy* 182 (2017) 44–53.